
Upper limb surface electromyography - geometry, spectral characteristics, temporal evolution, and demographic confounds

Harshavardhana T. Gowda

Department of Electrical and Computer Engineering
University of California
Davis, CA 95616
tgharshavardhana@gmail.com

Neha Kaul

Center for Mind & Brain
University of California
Davis, CA 95616
nkaul@ucdavis.edu

Carlos Carrasco

Neuroscience Graduate Group
University of California
Davis, CA 95616
cdcarrasco@ucdavis.edu

Marcus A. Battraw

Department of Mechanical and Mechatronic Engineering and Advanced Manufacturing
California State University
Chico, CA 95929
mbattraw@csuchico.edu

Safa Amer, Saniya Kotwal, Selena Lam, Zachary McNaughton, Ferdous Rahimi, Sana Shehabi

Center for Mind & Brain
University of California
Davis, CA 95616

Jonathon S. Schofield

Department of Mechanical and Aerospace Engineering
University of California
Davis, CA 95616
jschofield@ucdavis.edu

Lee M. Miller

Center for Mind and Brain*
University of California
Davis, CA 95616
leemiller@ucdavis.edu

Abstract

Brain-body-computer interfaces aim to provide a fluid and natural way for humans to interact with technology. Among noninvasive interfaces, surface electromyogram (sEMG) signals have shown particular utility. However, much remains unknown about how sEMG is affected by various physiological and anatomical factors and how these confounds might affect gesture decoding across individuals or groups. In this article, we show that sEMG signals evince non-Euclidean graph data structure that is defined by a set of orthogonal axes and explain the signal distribution shift across individuals. We provide a dataset of upper limb sEMG signals and physiological measures of 91 adults as they perform 10 different hand gestures. Participants were selected to be representative of various age groups (18

*Lee M. Miller is also associated with the Department of Neurobiology, Physiology, and Behavior and the Department of Otolaryngology-Head and Neck Surgery

to 92 years) and BMI (healthy, overweight, and obese). Additional anatomical or physiological measures that might impact sEMG signals were also collected, such as skin hydration and elasticity. The article describes the inherent structure of sEMG data and provides methods to construct differentiable signal features that can be used with machine learning algorithms that use backpropagation. We then analyze how those parameters correlate with various physiological measures to probe if they can induce bias against (or towards) certain population groups. We find that higher frequencies in sEMG, although comprising less power than lower ones, provide better gesture decoding and show less bias with regard to demographic, circumstantial, and physiological confounds (such as age, skin hydration, and skin elasticity).

1 Introduction

Electromyogram signals measured at the surface of the skin can detect muscle activation patterns and their corresponding physical movements. Humans use hand gestures as one of the prominent means for communication and interaction. Therefore, neural interfaces designed to leverage sEMG signals from the upper limb can facilitate a wide range of applications such as hand-gesture based computer interfaces, handwriting decoding, keyboard typing, and even supernumerary limb or finger augmentation. However, a crucial barrier for deploying such neural interfaces at scale across the general population is that sEMG signals differ significantly across individuals and sessions due to varying anatomy and physiology. Little is known about how such demographic characteristics affect the sEMG signals, and therefore how they might affect decoding performance. Here, we show that sEMG signals are defined by a set of orthogonal axes and that the signal distribution shift is defined by the change of basis.

Previous reports [4] and [3] provide a detailed description of how sEMG signals depend on the neural drive and muscle properties. In [4], authors model sEMG signals as an interference signal expressed as summations of motor unit action potentials weighted by neural drive signals. The measurement of action potentials depends on various characteristics which may differ widely across individuals such as thickness of subcutaneous fat, spatial distribution of muscle fibers, distribution of muscle fiber conduction velocity [4] and circumstantial factors such as electrode locations. sEMG signals are also influenced by neural properties such as discharge characteristics of the neural drive [4], which again, may vary across individuals and circumstances. It is not feasible to disentangle the influence of individual physiological properties on sEMG signals as such properties cannot be independently controlled in an experimental setting.

Due to the confounds mentioned above, it is generally not possible to study sEMG signals in humans via deterministic models. Widely used hand-crafted features as in [8] vary substantially across the population (refer to [3] and [4] for description of how global characteristics of sEMG signals such as signal power, amplitude, and spectra are confounded by physiological factors). Therefore, classification techniques based on such hand-crafted features are brittle and cannot generalize beyond discrete classification problems in experimental settings.

To deploy sEMG-based non-invasive neural interfaces at scale in the general population, one must be able to capture informative representations of the sEMG signals that enable rapid adaptation under new contexts (physiological, situational) via few-shot or transfer learning. By way of example, audio – another biologically produced signal that differs across individuals and circumstances for the same linguistic content – when trained using deep-learning algorithms as in [1] and [6] produces meaningful representations that provide state-of-the-art performance on downstream tasks such as automatic speech recognition. It should be noted that such deep-learning algorithms generalize across populations with varying physiology of vibratory (the vocal folds) and resonating systems (the supraglottic airway and vocal tract). This serves as a template to develop machine-learning algorithms for sEMG signals without deterministic modeling of underlying physiology of neural drive and action potentials. However, sEMG signals differ from audio signals in that sEMG signals are defined by a set of orthogonal axes as opposed to being sampled on a single dimension. Therefore, convolutional neural networks, which form the feature extraction layers in [1] and [6] by leveraging

the statistical properties of audio signals on a 1D line (audio being a function in the Euclidean space sampled on a line) using shared parameters in the convolutional layers, dilations, and downsampling (local pooling) do not generate appropriate inductive bias for non-Euclidean sEMG data. We therefore adapt neural network architecture described in [7] that leverages the geometric priors appropriate for sEMG signals and effectively learns the manifold-valued data.

In this article, we show that the differentiable manifold of symmetric positive definite (SPD) matrices effectively models the multivariate relationships among various muscle sites and naturally encodes discerning information to decode different hand movements. We also characterize the relative merits of different frequency bands in the sEMG signal, both for decoding accuracy and robustness against demographic factors. We show that confounding inter-individual signal differences occur at lower sEMG frequencies, whereas higher frequencies provide a feature subspace that generalizes well and remains relatively unbiased across population groups.

2 Data description

A total of 91 subjects (age range: 18–92 years; mean age 53.53; 37 males and 54 females) participated in our study (see *ethical statement* section for detailed subject selection criteria). Forearm sEMG was collected from the upper limb using 12 electrodes. Eight electrodes were placed equally spaced around the main belly of the forearm muscles below the elbow at approximately 1/3 the distance from elbow to wrist. Four electrodes were placed equally spaced around the wrist joint (figure 1). Each subject performed ten different hand gestures (figure 2), with each gesture performed thirty-six times. Ten gestures are labeled as follows: 1 - Down, 2 - Index finger pinch, 3 - Left, 4 - Middle finger pinch, 5 - Index point, 6 - Power grasp, 7 - Right, 8 - Two finger pinch, 9 - Up, 10 - Splay.

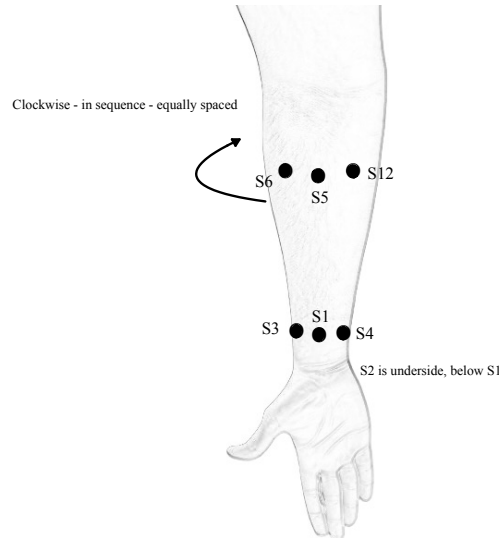


Figure 1: Sensors are named with a prefix S followed by the sensor number. 4 sensors are placed equally spaced around the wrist joint ($S1$, $S3$, $S4$ are shown. $S2$ is on the underside, below $S1$). Sensors $S5$ to $S12$ are placed equally spaced around the belly of the forearm. Sensors $S5$ and $S6$ are shown. The rest of the sensors are equally spaced around the forearm in the clockwise direction so that $S12$ is adjacent to $S5$ as shown.

2.1 Data acquisition protocol

sEMG was acquired with Delsys Trigno double differential sEMG electrodes (Delsys, Inc) and NI USB-6210 multifunction I/O (National Instruments Corporation — 16-inputs, 16-bit, 250kS/s) data acquisition system at a rate of 2000 Hertz or 2148 Hertz. Data from the Delsys electrodes were transmitted wirelessly to a base station, which then relayed the information to a computer via a USB connection using the NI USB-6210 data acquisition system. A graphical user interface

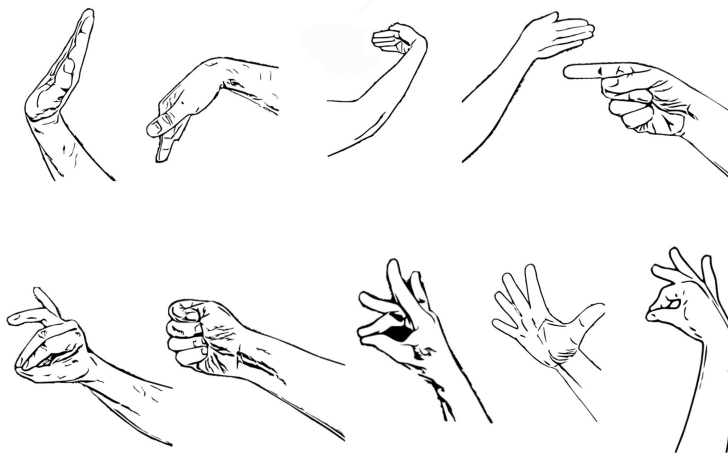


Figure 2: Ten gestures included in the experiment. From top-left: up, down, left, right, index point, two finger pinch, power grasp, middle finger pinch, splay, index finger pinch.

(GUI) was developed to display hand gestures on a screen. Subjects, comfortably seated with their dominant forearm resting on an elevated platform on the table, performed the displayed gestures. They could choose their resting position and change it throughout the experiment as needed. Each gesture was displayed for 2 seconds, followed by a 2-second resting period. During the 2-second gesture display, subjects were instructed to perform the gesture. Subjects were instructed to rest during the subsequent blank screen.

The experiment was divided into six sessions, each consisting of sixty trials with six repetitions of ten different gestures. The order of gestures within each session was pseudorandomly generated to assess how variations in gesture performance affect decoding accuracy. This approach prevented repetitive, unconscious, and unnaturally consistent movements that could occur if all repetitions of a gesture were performed sequentially. In total, each subject completed 360 trials. We used ZeroMQ sockets (<https://zeromq.org/socket-api/>) and Lab Streaming Layer (<https://github.com/sccn/labstreaminglayer>) in Python to time-sync GUI instructions with data streamed from the Delsys system. Data streams were synced to the master clock on the computer that received both sEMG data and event markers from the GUI.

We collected demographic and physiological measures such as age, height, weight, subcutaneous fat in the forearm, hair density on the forearm, elasticity of the skin on the forearm, and the moisture of the skin on the forearm. Age, height, and weight were self-reported. We measured the elasticity of forearm skin using Delfin Elastimeter (<https://delfintech.com/products/elastimeter/>), and skin moisture of the forearm using Delfin MoisturemeterSC (<https://delfintech.com/products/moisturemetersc/>). Hair density was determined using an Aram Huvis API 202 device (<https://www.aramhuvis.com/en/api/>) on 4 arm locations - wrist anterior, wrist posterior, upper arm anterior, and upper arm posterior. We measured subcutaneous fat on 2 arm locations - wrist posterior and forearm posterior using a body fat caliper (by MEDCA). Distribution of age, BMI, elasticity, and hydration is shown in figure 3. Subcutaneous fat measured using fat caliper and hair density distribution on the forearm did not show significant variability within the population group.

2.2 Data format

We make the data publicly available in `pickle` (`.pk1`) format. The data file is formatted as a Python dictionary which consists of four main keys:

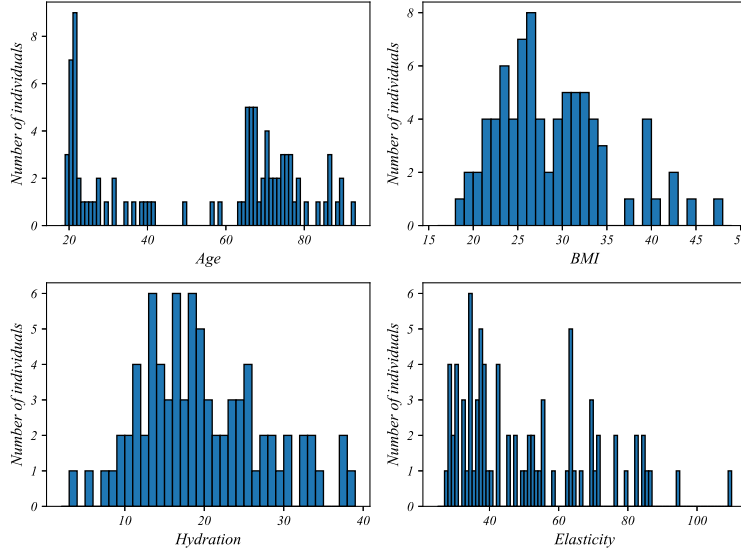


Figure 3: Distribution of age, BMI, elasticity, and hydration

- **EMG** - contains the sEMG data (a numpy array) of shape $(360, 12, \tau)$. τ is the number of timepoints corresponding to a duration of 2 seconds, which is 4000 or 4296 sample points (depending on whether sEMG was sampled at 2000 or 2148 Hertz). Subjects performed 360 trials over 6 different sessions with each session consisting of 60 trials. sEMG was collected from 12 electrodes (see figure 1 for electrode positions).
- **Labels** - contains labels corresponding to the gestures in EMG. It is a numpy array of shape $(360,)$.
- **Frequency** - an integer that indicates the frequency at which sEMG was sampled (2000 or 2148 Hertz).
- **Physiology** - a *dictionary* containing physiological and demographic measures.
 - **Age** - an integer that indicates the self-reported age of the subject in years.
 - **Height** - a float that indicates the self-reported height of the subject in centimeters.
 - **Weight** - a float that indicates the self-reported weight of the subject in kilograms.
 - **Skin_Hydration** - a float that indicates the moisture level of the forearm skin (for measurement units, range, and calibration, please refer to <https://delfintech.com/products/moisturemeters/>).
 - **Skin_Elasticity** - a float that indicates the elasticity of the forearm skin in Nm^{-1} .
 - **Subcutaneous_Fat** - a list containing the measured subcutaneous fat in the forearm. Four measurements were taken from forearm anterior, forearm posterior, wrist anterior, and wrist posterior. They are presented in the same order in the list in millimeters.
 - **Hair_Density** - a list containing hair density measurements on the forearm. Two measurements were taken on the forearm anterior and the wrist anterior. They are presented in the same order in the list in $\text{hairs}(\text{cm})^{-2}$.
 - **Sex** - self-reported sex (biological). F - Female. M - Male. N - Other (non-binary).

If certain physiological measures do not exist for a given individual, they are tagged with placeholder None.

3 Methods

Multiple muscles work in a synchronous manner to execute a given hand gesture and these synergistic muscle activation patterns show graph data structure with distinct functional connectivity for different gestures. In our previous work ([5]), we showed that the SPD matrices constructed by computing

pairwise signal covariances among spatially separated sensor electrodes on the upper limb effectively encode the functional connectivity of the underlying neuromuscular system. We briefly recall some of the formulations in [5] here. We adapt the methods from [10] to analyse SPD matrices via Cholesky decomposition on a Riemannian manifold. An SPD matrix \mathcal{E} is mapped to the Cholesky space via a bijective mapping \mathcal{L} . A mapping $\widetilde{\text{Log}}$, maps a matrix L on the Cholesky manifold to the tangent space. A mapping $\widetilde{\text{vec}}$, vectorizes the matrix X in the tangent space of the Cholesky manifold (equivalent to $L[\text{numpy.tril_indices}(\text{len}(L))]$). \mathcal{S} , $\widetilde{\text{Exp}}$, and invvec are the inverse operations of \mathcal{L} , $\widetilde{\text{Log}}$, and $\widetilde{\text{vec}}$ respectively. The mapping operations are summarized below.

$$\mathcal{E} \xrightleftharpoons[\mathcal{S}]{\mathcal{L}} L \xrightleftharpoons[\widetilde{\text{Exp}}]{\widetilde{\text{Log}}} X \xrightleftharpoons[\text{invvec}]{\text{vec}} x. \quad (1)$$

For classifying the hand gestures, we use minimum distance to mean (MDM), k -medoids, and SVM algorithms using Riemannian distance and Fréchet mean as defined in [10]. For the description of these algorithms, refer to [5]. Additionally, for SPD matrix learning on the manifold, we adapt the model in [7]. The architecture of the model is shown in figure 4. We briefly describe the core formulations in [7] here.

The neural network architecture designed for learning discriminative SPD matrix representations is made of three types of layers. The first type is a linear transformation layer where, at the k -th layer, an input SPD matrix \mathcal{E}_{k-1} of size $c_{k-1} \times c_{k-1}$ is transformed according to the relation $\mathcal{E}_k = W_k^T \mathcal{E}_{k-1} W_k$. The transformation matrix W_k , of dimensions $c_{k-1} \times c_k$, produces an output SPD matrix \mathcal{E}_k of size $c_k \times c_k$. The matrix W_k is constrained to be semi-orthogonal, satisfying $W_k^T W_k = I$, and belongs on a Stiefel manifold. The second type is a non-linear layer, which modifies the eigendecomposition of \mathcal{E}_{k-1} by computing $\mathcal{E}_k = U_{k-1} \max(\epsilon I, \Sigma_{k-1}) U_{k-1}^T$, where U_{k-1} and Σ_{k-1} are the eigenvector and eigenvalue matrices of \mathcal{E}_{k-1} , and ϵ is a small positive constant. The final layer type maps SPD matrices from the manifold space to the tangent space, allowing Euclidean operations. This is achieved by $\mathcal{E}_k = U_{k-1} \log(\Sigma_{k-1}) U_{k-1}^T$, where $\log(\Sigma_{k-1})$ represents the element-wise logarithm of the eigenvalue matrix Σ_{k-1} .

For backpropagation, the gradient of the loss function L with respect to W_k , when restricted to the tangent space of the Stiefel manifold (denoted by $\mathbb{R}^{c_{k-1} \times c_k}$, the space of all full-rank matrices of dimension $c_{k-1} \times c_k$) is given by

$$\nabla L_{W_k}^{(k)} = \nabla L_{W_k(\text{Euclidean})}^{(k)} - W_k \nabla L_{W_k(\text{Euclidean})}^{T(k)} W_k.$$

The gradient is updated as

$$W_k \leftarrow W_k - \lambda \nabla L_{W_k}^{(k)},$$

where λ is the learning rate. W_k is then mapped back to the Stiefel manifold (from the tangent space) via orthogonalization. We use Gram-Schmidt method for matrix orthogonalization. Refer to [7] for backpropagation through non-linear and tangent space mapping layers.

In figure 5 (left), we show that the SPD matrices of hand gestures are naturally distinguishable on a cone manifold. Within a given individual, any given gesture \mathcal{E} can be expressed as $\mathcal{E} = Q \Sigma Q^T$ such that Σ is approximately diagonal. We train the model in figure 4 separately for each subject and analyse the learned weights. The orthogonal weight matrix $W_{12 \times 12}^{(1)}$ learned by the model approximately diagonalizes the SPD matrix $\mathcal{E}_{12 \times 12}^{(0)}$ for any given gesture. The ratio of the absolute values of maximum non-diagonal value to maximum diagonal value of $\mathcal{E}_{12 \times 12}^{(0)}$ and $\mathcal{E}_{12 \times 12}^{(1)}$ averaged over all 360 trials are shown in figure 14. That is, within an individual, all gestures have approximately the same eigenbasis vectors $Q = W^{(1)T}$. This implies, for the hardware with 12 sensor electrodes, any gesture can be expressed as a linear combination of 12 vectors, each with dimension 12 spanning the Euclidean space \mathbb{R}^{12} . The approximate Eigen basis vectors Q is different for different individuals (see figure 15). Therefore, the domain shift in sEMG signals can be described as the change of basis. Figure 15 reveals that the eigenbasis vectors defining the sEMG signals are almost unique implying that the combined effect of varying physiological, anatomical, and neural drive properties across individuals result in unique functional connectivity patterns. The classification accuracy of 10 hand gestures with various models are presented in table 6.

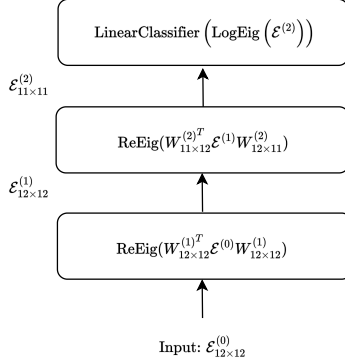


Figure 4: Neural network architecture for SPD matrix learning. ReEig is defined as $\mathcal{E}_k = U_{k-1} \max(\epsilon I, \Sigma_{k-1}) U_{k-1}^T$ and LogEig is defined as $\mathcal{E}_k = U_{k-1} \log(\Sigma_{k-1}) U_{k-1}^T$. The model has approximately 1500 trainable parameters.

Given that the signals within an individual have approximately the same eigenbasis vectors, SPD matrices of an individual can be mapped to the tangent space of the manifold without excessively distorting the geometric structure. In figure 5 (right), we show that such a mapping still preserves the inherent geometric structure and in figure 6, we show that the decoding accuracy using minimum distance to mean algorithm on the manifold and in the Euclidean space yield similar results.

In summary, signal covariances across spatially separated sensor electrodes naturally distinguish different hand movements and the model in figure 4 makes use of this manifold-valued geometric prior to parsimoniously (with just 1500 parameters) learn the spatial features of the data. The model in figure 4 is parameter efficient and performs better compared to convolutional neural networks defined on the Euclidean space (which expects signals to be sampled on 1-dimensional or 2-dimensional grids) [5]. Also, since the geometry is preserved when signals are mapped to the tangent space, such vector-embeddings are useful as inputs to transformers and recurrent neural networks. Furthermore, one can define recurrent neural networks on the manifold of SPD matrices and use manifold ordinary differential equations to capture the temporal dynamics of the sEMG signals as explained in [9].

Since the Euclidean space $\mathbb{R}^{\mathcal{V}}$, where \mathcal{V} is the number of sensor electrodes can be spanned by an infinite number of orthogonal vector sets, and as the set of orthogonal axes defining the sEMG signals of an individual are uniquely sampled from such a set (empirically demonstrated on 91 diverse subjects in figure 15), zero-shot learning of sEMG spatial patterns across subjects is intractable. This is unlike images and audio signals where multiscale hierarchical learning through stride convolutions and pooling lead to generalization (in case of images, multiscale dyadic clustering allows learning of fine-scale local features such as edges and textures and eventually the coarse-scale global features such as shapes and objects). However, sEMG signals do not show such a hierarchical structure of features, rather they are simply linear combinations of a set of orthogonal vectors.

4 Results

4.1 Structure of sEMG signals

SPD covariance matrices belonging to different gestures are inherently well separated (figure 5 - left). Additionally, mapping these SPD matrices to the tangent space and vectorizing them using relationships described in equation 1 still preserves this inherent structure (figure 5-right) as covariance matrices belonging to a given individual have the same approximate eigenbasis vectors. Also, when classifying the gestures, the minimum distance to mean (MDM) algorithm on the manifold of SPD matrices and MDM on the Euclidean space (on vectorized tangent mapped matrices) achieve similar performance (figure 6).

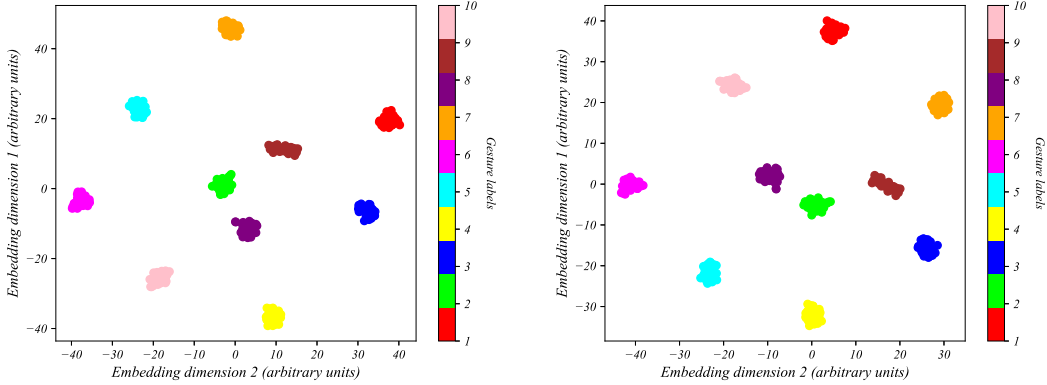


Figure 5: *Left*: t -SNE of covariance matrices using Riemannian distance for hand gestures of subject 80 (from 80_pk1). *Right*: t -SNE of vectorized tangent mapped covariance matrices (equation 1) using Euclidean distance for hand gestures of subject 80.

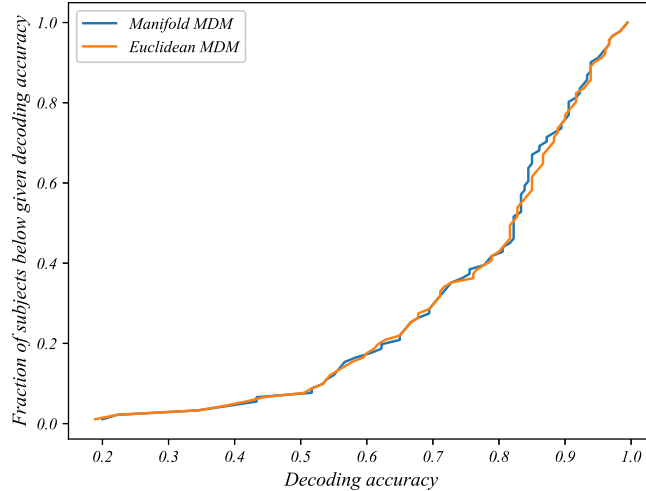


Figure 6: Decoding accuracy versus the fraction of subjects below a given decoding accuracy. It is a 10 way classification and chance decoding accuracy is 0.1. Train set and test set have equal number of gesture repetitions.

4.2 Spectral characteristics of sEMG signals

To characterize if certain spectral bands show better discerning structure for different hand gestures across population groups and circumstances (such as age, BMI, skin moisture, and elasticity), we analyze sEMG signals in four separate spectral bands - 20 to 50 Hz, 50 to 110 Hz, 110 to 230 Hz, and 230 to 450 Hz. We obtain these spectral bands by filtering the raw signals using third order Butterworth bandpass filter (using `scipy filtfilt`). We show that sEMG signal power is concentrated in the lower spectral bands (figure 7) and different spectral components encode similar discerning information about different hand movements (figure 8). That is, we can decode different gestures with high accuracy across different spectral bands. We show the decoding accuracy using MDM algorithm on the manifold of SPD matrices across different frequency bands in figure 9 and summarize the observations in table 1. Decoding accuracy is higher in the higher spectral bands even though lower spectral bands have more power.

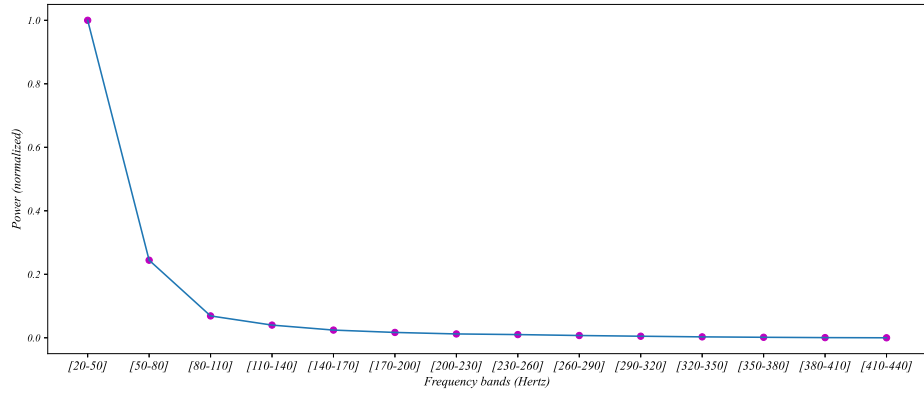


Figure 7: Power in various frequency bands. Filtered sEMG signals are squared to obtain power. Shown power is the average across all 91 subjects (within each individual, the power is averaged across all 12 sensor electrodes).

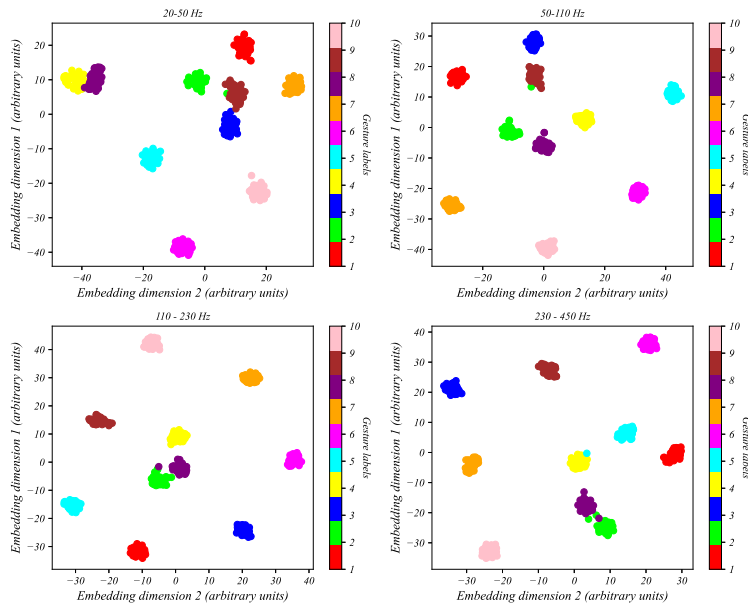


Figure 8: t -SNE of covariance matrices using Riemannian distance for hand gestures of subject 80 (from 80_pk1) in different spectral bands. We can see that covariance matrices cluster separately according to gestures in all spectral bands. That is, similar information is encoded in all bands. Embedding is colored according to gestures.

Spectral band	Decoding accuracy (50-50 train-test split)	Fraction of power
20 to 50 Hz	0.669	0.683
50 to 110 Hz	0.799	0.215
110 to 230 Hz	0.825	0.071
230 to 450 Hz	0.811	0.032

Table 1: Average summary values for figure 9. Average decoding accuracy and distribution of average power across all subjects in various spectral bands. It is a 10-way classification problem and the random decoding accuracy is 0.1.

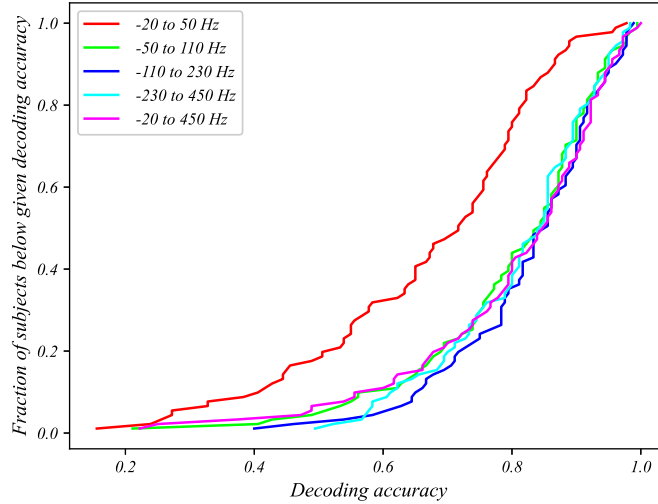


Figure 9: Decoding accuracy using manifold MDM in different spectral bands. It is a 10-way classification problem and the random decoding accuracy is 0.1. Train and test sets have equal number of gesture repetitions.

4.3 Effect of electrode positions on hand gesture decoding

We evaluate how sEMG signal information is encoded at various muscle locations, as this may inform optimal design for hand-based sEMG interfaces. We compare the decoding accuracy using 4 electrodes placed on the wrist ($S1$ to $S4$) and 8 electrodes placed around the forearm ($S5$ to $S8$) separately. Decoding accuracy using 4 wrist electrodes is shown in figure 10 with average values summarized in table 2. Decoding accuracy using 8 wrist electrodes is shown in figure 11 with average values summarized in table 3. We see that decoding using only 4 wrist electrodes results in inferior performance relative to the 8-channel forearm array, and that the best performance is achieved with all 12 electrode channels.

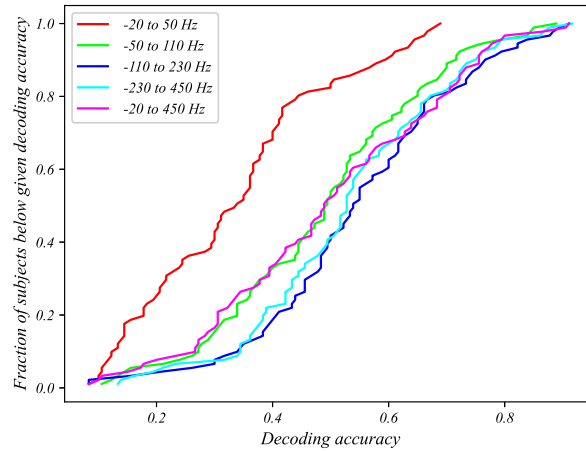


Figure 10: Decoding accuracy using manifold MDM in different spectral bands using only 4 electrodes on the wrist (electrodes $S1$, $S2$, $S3$, and $S4$). It is a 10-way classification problem and the random decoding accuracy is 0.1. Train and test sets have equal number of gesture repetitions.

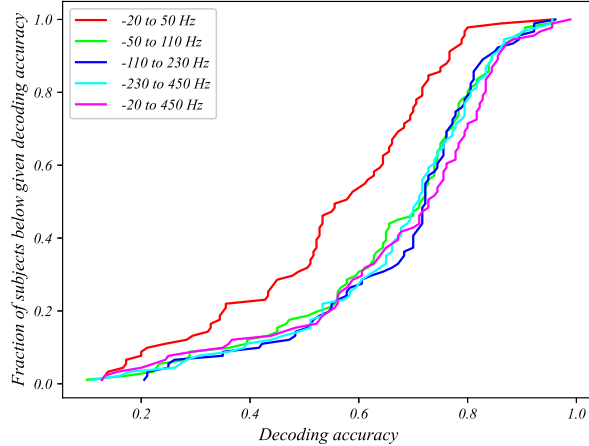


Figure 11: Decoding accuracy using manifold MDM in different spectral bands using only 8 electrodes on the forearm muscle belly (electrodes $S5$ to $S12$). It is a 10-way classification problem and the random decoding accuracy is 0.1. Train and test sets have equal number of gesture repetitions.

Spectral band	Decoding accuracy (50-50 train-test split)	Fraction of power
20 to 50 Hz	0.34	0.65
50 to 110 Hz	0.49	0.27
110 to 230 Hz	0.55	0.06
230 to 450 Hz	0.53	0.02

Table 2: Average summary values for figure 10 (with 4 wrist electrodes only). Average decoding accuracy and distribution of average power across all subjects in various spectral bands. It is a 10-way classification problem and the random decoding accuracy is 0.1.

Spectral band	Decoding accuracy (50-50 train-test split)	Fraction of power
20 to 50 Hz	0.55	0.69
50 to 110 Hz	0.66	0.19
110 to 230 Hz	0.67	0.07
230 to 450 Hz	0.67	0.04

Table 3: Average summary values for figure 11 (using 8 forearm electrodes only). Average decoding accuracy and distribution of average power across all subjects in various spectral bands. It is a 10-way classification problem and the random decoding accuracy is 0.1.

4.4 Temporal evolution of sEMG signals

An individual may follow different paths to perform a given gesture; that is, within a time-context window, one may perform a given gesture fast or slow or may reach the same end positions in different manners. Therefore, we study the evolution of sEMG signals to understand how the signal power and decoding accuracy (how discernible are different gestures at different time points) evolve during the gesture duration. The average power from all subjects and all trials across different time points is shown in figure 12. Cue to perform a gesture was given at time point $t = 0$. Negligible fraction of power is concentrated in the first 0.4 seconds and the last 0.4 seconds.

We can see that the decoding accuracy is low at around 0.8s (figure 13), the same time where signal power is maximum; we attribute this observation to muscle co-contractions that provide joint stability which is similar for all gestures. After 0.8s, we see that the decoding accuracy increases as we increase the time-context window. In figure 13, for all time-context window sizes for the duration of the gestures, decoding accuracy is well above the chance level. Furthermore, in congruence with the results in the previous section, higher frequency bands show better decoding performance across time-context windows.

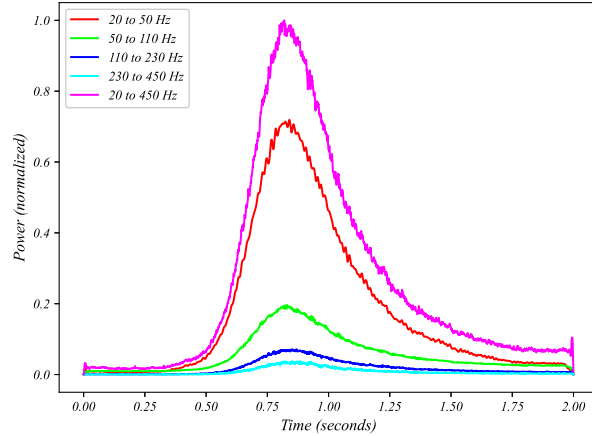


Figure 12: Time (for the entire duration of gestures, which is 2 seconds) versus normalized power. Power is averaged across all subjects and trials for a given time point (within each individual, the power is averaged across all 12 sensor electrodes).

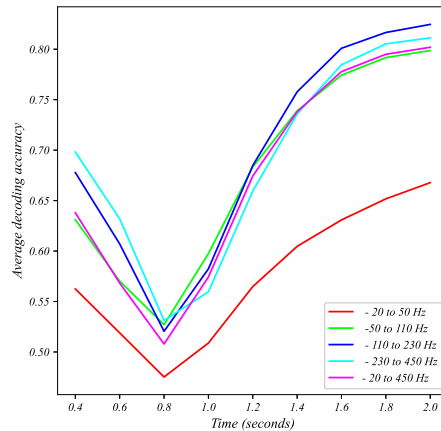


Figure 13: Average decoding accuracy across all subjects versus time context window. For example, decoding accuracy at $time = 0.5$ seconds is calculated by creating a covariance matrix by taking only the sample points belonging to $time < 0.5$ seconds (so, decoding accuracy at $time = 2s$ is calculated by considering all time points between 0 and 2 seconds). Cue for starting the gesture is given at $time = 0s$. Decoding is done using manifold MDM. It is a 10-way classification problem and the random decoding accuracy is 0.1.

4.5 Demographic confounds of sEMG signals

We explore if the inherent geometric structure of the sEMG signals (figure 5) is influenced by factors such as age, skin hydration, skin elasticity, and BMI. That is, we analyze if the geometric structure is pronounced (or unremarkable) in certain population groups. To access this, we make use of classification accuracy obtained using unsupervised k -medoids algorithm on the manifold as this algorithm encapsulates all the geometric structure of the data including how densely (or sparsely) the SPD matrices (belonging to a particular gesture) cluster on the manifold and how distinguishable (far apart) the clusters belonging to different gestures are and analyze the trends with respect to age, skin hydration, skin elasticity, and BMI.

We calculate variance inflation factor (VIF) for age, skin hydration, skin elasticity, and BMI to verify that no significant multicollinearity exists between these factors ². The values are summarized in table 4. The VIF values are well below 5 and do not show any problematic multicollinearity.

²using Python `statsmodels.stats.outliers_influence.variance_inflation_factor`

Feature	VIF
Age	2.20
Skin hydration	1.21
Skin elasticity	1.86
BMI	1.141

Table 4: Variance inflation factor (VIF) for features age, skin hydration, skin elasticity, and BMI.

We then perform multiple regression and find the linear relationship between the k -medoids decoding accuracy (dependent variable) and age, skin hydration, skin elasticity, and BMI (independent variables) using ordinary least square regression³. The proportion of variance the models explain (R^2) are summarized in table 5. We observe that the R^2 values are relatively low indicating that the variables age, skin hydration, skin elasticity, and BMI do not significantly explain the variance in the decoding accuracy. That is, the geometry of the sEMG signals is only slightly affected by these variables and higher frequencies are less confounded compared to lower frequencies. Also, as indicated by the p -values, only the model for frequency range 20 to 50 Hz is statistically significant. That is, at least one independent variable meaningfully explains the variability in the dependent variable in that frequency range. In all other frequency ranges, the models are not statistically significant (no independent variable meaningfully explains the variability in the dependent variable). Detailed regression model parameters are given in appendix B.

Frequency	R^2	p -value
20 to 50 Hz	0.148	0.0164
50 to 110 Hz	0.069	0.245
110 to 230 Hz	0.027	0.721
230 to 450 Hz	0.043	0.501

Table 5: Proportion of variance in decoding accuracy explained by age, skin hydration, skin elasticity, and BMI, with corresponding p -values.

In conclusion, sEMG signals evince geometric structure that allows simple and efficient decoding of different hand movements (table 6) and this inherent structure is largely unaffected by the variables such as age, skin hydration, skin elasticity, and BMI (table 5). However, the underlying functional graph connectivity is unique for all individuals (figure 15). That is, the set of orthogonal axes defining the sEMG signals are different for different individuals.

5 Discussion

The first and perhaps the most foundational result from this work is that even across such a varied population, sEMG retains an inherent geometric structure. Specifically, we show that covariance matrices are the natural descriptors of spatial activity of sEMG signals, in that they provide a compact and structured representation of different gestures on a Riemannian manifold.

In addition to the natural structure of sEMG gestures on the manifold of SPD matrices, we observe that not all frequencies of sEMG are equivalent. Decoding accuracy is higher in the higher spectral bands although lower frequency bands contain more signal power. Lower frequency bands are likely corrupted by signal artifacts, e.g. related to motion and relative movements between the skin surface and electrodes (which can change the skin impedance) [2]. Lower frequency bands are more confounded by demographic and physiological factors compared to higher spectral bands. Higher frequency bands therefore offer high decoding performance that is relatively unbiased with regard to age, BMI, and other demographic characteristics.

In an effort to determine how electrode location or configuration affects decoding, we compared the full electrode array to subsets: four around the wrist and eight around the forearm muscle bellies.

³using Python `statsmodels.regression.linear_model.OLS`

Forearm electrodes clearly outperform the wrist electrodes, which is perhaps unsurprising given the paucity of musculature in the wrist. However, decoding solely using wrist electrodes was still very much above chance. And while decoding with only 8 forearm electrodes provides reasonable accuracy, it is significantly less than that of all 12 electrodes. This suggests that an sEMG interface designed to be worn on the wrist, e.g. in a smart watch, should be augmented with sensors on the forearm muscle belly to maximize performance.

We next analyzed the temporal characteristics of sEMG signals. We demonstrate that there exists a window of poor decoding accuracy around gesture onset. This is likely due to muscle cocontractions for stabilizing joints around gesture onset which evince similar sEMG signal patterns for different gestures. The temporal dip in decoding performance has relevance for the latency or speed at which such decoding can identify subsequent individuated gestures. It remains to be seen whether such cocontractions also characterize time windows during dynamic, fluid gestures such as typing.

Finally, we provide an analysis of how various demographic and anatomical factors relate to sEMG signals and decoding accuracy. In general, geometric structure of sEMG is relatively insensitive to the factors we measured: age, height, weight, subcutaneous fat in the forearm, hair density on the forearm, elasticity of the skin on the forearm, and the moisture of the skin on the forearm. However we find that lower spectral components of sEMG are more confounded by demography and physiology compared to higher spectral components (table 5). Thus, sEMG decoding algorithms that seek to be unbiased, equitable, and broadly accessible should relegate decoding to these higher frequencies.

We hope that the open-sourced data, codes, and methods provided here inform the future research in the area of non-invasive sEMG based neural interfaces and its equitable access across population groups.

Acknowledgments and Disclosure of Funding

This work was supported by Meta Platforms Technologies (Facebook Research) with an award to LMM through the Ethical Neurotechnology program and by the University of California Davis School of Medicine Cultivating Team Science Award to LMM. We would like to thank Stephanie Naufel at Facebook Reality Labs for her valuable guidance.

HTG is supported by Neuralstorm Fellowship, NSF NRT Award No. 2152260 and Ellis Fund administered by the University of California, Davis.

Data and code availability

Codes are available at <https://github.com/HarshavardhanaTG/wristEMG>.

Data is available at <https://osf.io/3kzcb/>.

Ethical statement

Research was conducted in accordance with the principles embodied in the Declaration of Helsinki and in accordance with the University of California Davis Institutional Review Board Administration protocol 2078695-1. All participants provided written informed consent. Consent was also given for publication of the deidentified data by all participants. Participants were healthy volunteers and were selected from any gender and all ethnic and racial groups. Subjects were aged 18 or above, were able to fully understand spoken and written English, and were capable of following task instructions. Subjects had no skin conditions or wounds where electrodes were placed. Subjects were excluded if they had uncorrected vision problems or neuromotor disorders that prevented them from making hand gestures. Children, adults who were unable to consent, and prisoners were not included in the experiments.

Author contributions

- H.T.G. - Mathematical formulation, concepts development, data analysis, experiment design, data collection software design, data collection, manuscript preparation.
- N.K. - Data collection.
- C.C. - Data collection, experiment design.
- M.B. - Experiment design.
- S.A., S. K., S. L., Z. M., F. R. - Data collection.
- S.S. and H.T.G - Analyzed demographic confounds (section 4.6).
- J.S. - Concepts development, experiment design, manuscript review.
- L.M.M. - Concepts development, experiment design, manuscript preparation.

References

- [1] Alexei Baevski, Yuhao Zhou, Abdelrahman Mohamed, and Michael Auli. wav2vec 2.0: A framework for self-supervised learning of speech representations. *Advances in neural information processing systems*, 33:12449–12460, 2020.
- [2] Edward A Clancy, Evelyn L Morin, and Roberto Merletti. Sampling, noise-reduction and amplitude estimation issues in surface electromyography. *Journal of electromyography and kinesiology*, 12(1):1–16, 2002.
- [3] Dario Farina, Roberto Merletti, and Roger M Enoka. The extraction of neural strategies from the surface emg. *Journal of applied physiology*, 96(4):1486–1495, 2004.
- [4] Dario Farina, Roberto Merletti, and Roger M Enoka. The extraction of neural strategies from the surface emg: an update. *Journal of applied physiology*, 117(11):1215–1230, 2014.

- [5] Harshavardhana T Gowda and Lee M Miller. Topology of surface electromyogram signals: hand gesture decoding on riemannian manifolds. *Journal of Neural Engineering*, 2024.
- [6] Wei-Ning Hsu, Benjamin Bolte, Yao-Hung Hubert Tsai, Kushal Lakhotia, Ruslan Salakhutdinov, and Abdelrahman Mohamed. Hubert: Self-supervised speech representation learning by masked prediction of hidden units. *IEEE/ACM transactions on audio, speech, and language processing*, 29:3451–3460, 2021.
- [7] Zhiwu Huang and Luc Van Gool. A riemannian network for spd matrix learning. In *Proceedings of the AAAI conference on artificial intelligence*, volume 31, 2017.
- [8] B Hudgins, P Parker, and RN Scott. A new strategy for multifunction myoelectric control. *IEEE transactions on biomedical engineering*, 40(1):82–94, 1993.
- [9] Seungwoo Jeong, Wonjun Ko, Ahmad Wisnu Mulyadi, and Heung-II Suk. Deep efficient continuous manifold learning for time series modeling. *IEEE Transactions on Pattern Analysis and Machine Intelligence*, 2023.
- [10] Zhenhua Lin. Riemannian geometry of symmetric positive definite matrices via cholesky decomposition. *SIAM Journal on Matrix Analysis and Applications*, 40(4):1353–1370, 2019.

Appendix A

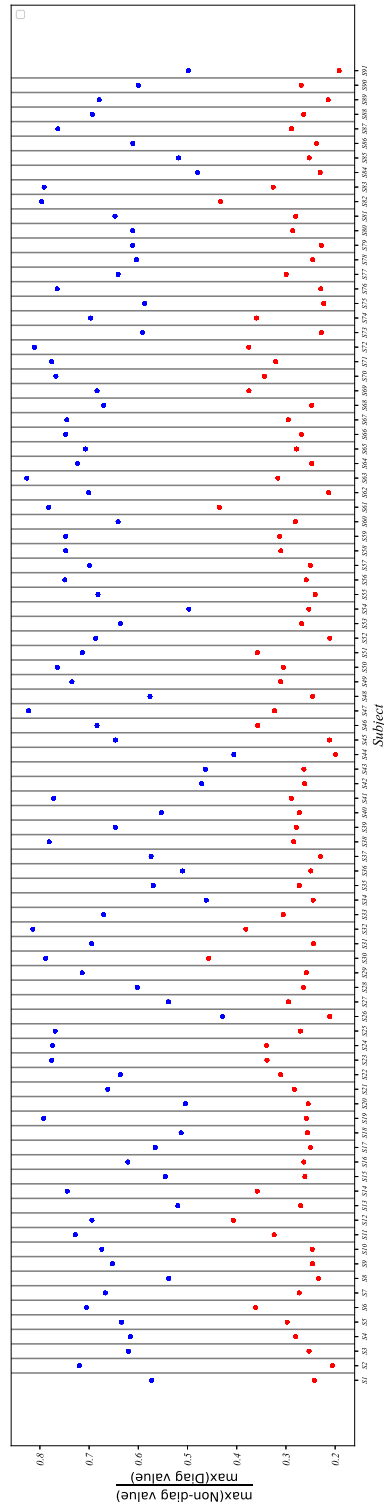


Figure 14: All gesture of an individual have approximately the same eigenbasis vectors. Blue - $\frac{\max(\text{non-diagonal}(\text{abs}(\mathcal{E}^{(0)})))}{\max(\text{diagonal}(\mathcal{E}^{(0)}))}$ averaged over all 360 trials of a given individual. Red - $\frac{\max(\text{non-diagonal}(\text{abs}(\mathcal{E}^{(1)})))}{\max(\text{diagonal}(\mathcal{E}^{(1)}))}$ averaged over all 360 trials of a given individual.

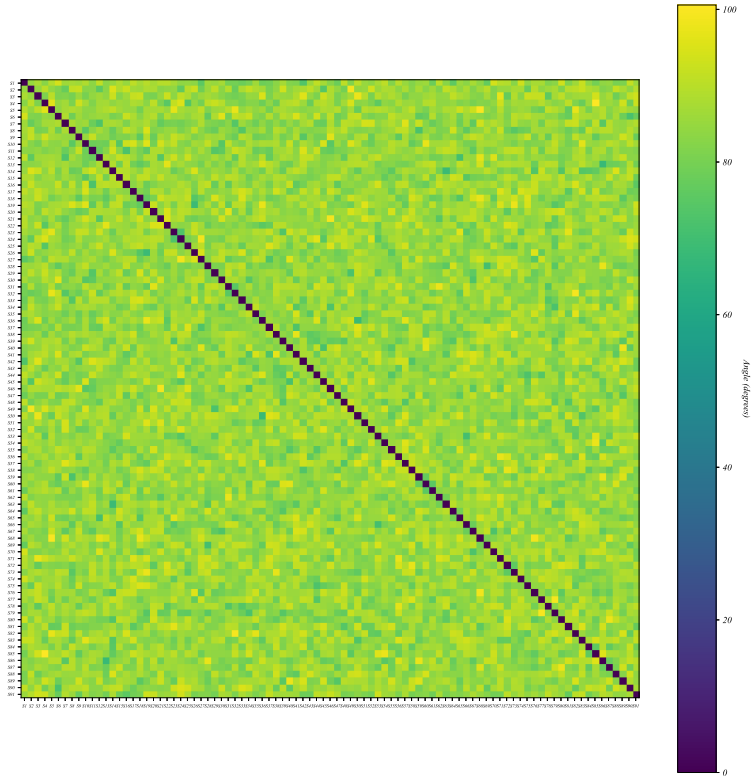


Figure 15: Gestures differ substantially across individuals. Approximate eigenbasis vectors ($Q = W_{12 \times 12}^{(1)}$) are different for different individuals.

$$\theta = \cos^{-1} \left(\frac{\text{trace}(Q_i Q_j^T)}{\sqrt{\text{trace}(Q_i Q_i^T)} \sqrt{\text{trace}(Q_j Q_j^T)}} \right)$$

between approximate eigenbasis matrices Q_i and Q_j of different individuals i and j .

Subject	k -medoids	MDM		SVM ($\gamma = 1$)		Model in figure 4	
		Split A	Split B	Split A	Split B	Split A	Split B
1	0.503	0.711	0.778	0.761	0.789	0.756	0.822
2	0.747	0.850	0.833	0.878	0.867	0.867	0.911
3	0.486	0.650	0.644	0.661	0.711	0.661	0.811
4	0.867	0.906	0.911	0.933	0.944	0.950	0.944
5	0.378	0.622	0.689	0.611	0.722	0.622	0.733
6	0.708	0.850	0.811	0.856	0.789	0.878	0.878
7	0.192	0.200	0.300	0.239	0.289	0.267	0.389
8	0.578	0.650	0.656	0.689	0.644	0.711	0.711
9	0.408	0.561	0.600	0.617	0.644	0.572	0.656
10	0.511	0.667	0.756	0.717	0.778	0.722	0.800
11	0.361	0.694	0.767	0.778	0.800	0.706	0.789
12	0.631	0.839	0.811	0.833	0.889	0.861	0.922
13	0.181	0.344	0.422	0.350	0.400	0.361	0.433
14	0.900	0.906	0.967	0.939	0.933	0.944	0.944
15	0.558	0.756	0.822	0.794	0.844	0.789	0.844
16	0.861	0.894	0.900	0.933	0.944	0.922	0.933
17	0.525	0.583	0.744	0.694	0.867	0.722	0.911
18	0.358	0.694	0.778	0.733	0.822	0.761	0.844
19	0.650	0.833	0.856	0.856	0.900	0.861	0.911
20	0.183	0.433	0.478	0.450	0.544	0.483	0.489
21	0.822	0.844	0.922	0.894	0.944	0.889	0.922
22	0.797	0.928	0.956	0.933	0.956	0.961	0.978
23	0.925	0.956	0.978	0.972	0.989	0.989	1.000
24	0.661	0.967	0.989	0.900	0.978	0.983	1.000
25	0.972	0.983	0.978	0.994	1.000	0.989	0.989
26	0.475	0.717	0.711	0.744	0.733	0.722	0.778
27	0.367	0.539	0.600	0.500	0.578	0.611	0.678
28	0.592	0.700	0.656	0.711	0.844	0.733	0.867
29	0.797	0.839	0.856	0.911	0.911	0.933	0.922
30	0.983	0.989	1.000	0.983	1.000	0.994	1.000
31	0.714	0.822	0.944	0.811	0.967	0.889	0.978
32	0.908	0.939	0.956	0.956	0.978	0.961	1.000
33	0.797	0.872	0.856	0.900	0.922	0.917	0.944
34	0.589	0.728	0.744	0.767	0.778	0.739	0.822
35	0.411	0.661	0.767	0.689	0.833	0.672	0.822
36	0.197	0.433	0.489	0.489	0.556	0.467	0.533
37	0.589	0.806	0.778	0.883	0.856	0.878	0.900
38	0.828	0.844	0.878	0.906	0.900	0.917	0.911
39	0.783	0.961	0.944	0.972	0.944	0.978	0.956
40	0.261	0.556	0.644	0.556	0.700	0.606	0.678
41	0.672	0.722	0.756	0.800	0.900	0.794	0.811
42	0.172	0.222	0.289	0.239	0.278	0.250	0.300
43	0.281	0.389	0.344	0.356	0.256	0.417	0.367
44	0.417	0.678	0.744	0.711	0.789	0.744	0.800
45	0.767	0.906	0.933	0.911	0.978	0.972	0.978
46	0.739	0.806	0.844	0.844	0.889	0.856	0.933
47	0.867	0.933	0.944	0.944	0.944	0.939	0.944
48	0.894	0.906	0.967	0.956	0.967	0.950	1.000
49	0.711	0.744	0.900	0.778	0.911	0.844	0.933
50	0.711	0.833	0.878	0.889	0.900	0.878	0.911
51	0.794	0.817	0.878	0.856	0.933	0.883	0.933
52	0.753	0.872	0.922	0.922	0.922	0.911	0.956
53	0.739	0.822	0.789	0.872	0.878	0.883	0.944
54	0.619	0.844	0.856	0.861	0.889	0.839	0.889
55	0.622	0.789	0.778	0.806	0.811	0.778	0.789

56	0.931	0.950	0.922	0.972	0.956	0.967	0.922
57	0.725	0.844	0.822	0.844	0.856	0.878	0.900
58	0.644	0.822	0.822	0.844	0.889	0.878	0.900
59	0.497	0.567	0.633	0.661	0.700	0.683	0.767
60	0.758	0.922	0.911	0.933	0.956	0.939	0.956
61	0.853	0.850	0.856	0.889	0.933	0.922	0.944
62	0.347	0.533	0.511	0.572	0.589	0.628	0.678
63	0.611	0.822	0.856	0.844	0.900	0.900	0.933
64	0.717	0.833	0.822	0.867	0.911	0.878	0.944
65	0.717	0.822	0.800	0.889	0.900	0.900	0.878
66	0.703	0.933	0.956	0.939	0.956	0.933	0.978
67	0.914	0.883	0.889	0.917	0.911	0.939	0.967
68	0.258	0.550	0.689	0.550	0.711	0.578	0.778
69	0.533	0.778	0.844	0.822	0.856	0.806	0.889
70	0.828	0.833	0.811	0.894	0.956	0.872	0.967
71	0.678	0.783	0.811	0.861	0.900	0.861	0.922
72	0.986	0.994	1.000	1.000	1.000	1.000	1.000
73	0.714	0.894	0.944	0.906	0.967	0.922	0.967
74	0.939	0.972	0.978	0.989	0.989	0.983	0.989
75	0.475	0.606	0.700	0.694	0.789	0.672	0.756
76	0.608	0.622	0.700	0.756	0.778	0.789	0.811
77	0.600	0.756	0.811	0.828	0.844	0.828	0.889
78	0.739	0.922	0.989	0.933	1.000	0.961	0.989
79	0.625	0.822	0.811	0.856	0.833	0.861	0.900
80	0.875	0.939	0.944	0.967	0.944	0.972	0.967
81	0.739	0.939	1.000	0.950	1.000	0.989	1.000
82	0.933	0.967	0.978	0.972	0.989	0.978	0.989
83	0.736	0.917	0.922	0.944	0.989	0.967	0.967
84	0.556	0.656	0.689	0.717	0.722	0.728	0.744
85	0.700	0.861	0.911	0.922	0.967	0.928	0.956
86	0.358	0.517	0.489	0.633	0.789	0.628	0.833
87	0.706	0.900	0.933	0.928	0.956	0.944	0.978
88	0.728	0.833	0.733	0.844	0.800	0.872	0.800
89	0.761	0.861	0.867	0.872	0.911	0.911	0.933
90	0.231	0.517	0.533	0.456	0.533	0.517	0.644
91	0.581	0.706	0.722	0.000	0.000	0.817	0.889
Mean	0.639	0.769	0.798	0.791	0.829	0.813	0.859

Table 6: Decoding accuracy of 10 hand gestures with various models. Random decoding accuracy is 0.1. All methods are defined on a cone manifold using Riemannian geodesic distance. Refer to [5] for the description of k -medoids, MDM, and SVM on the manifold. In *Split A*, train and test data sizes are equal — 18 instances of each gesture repetition are used for training and 18 instances of each gesture repetition are used for testing. In *Split B*, 27 instances of each gesture repetition are used for training and 9 instances of each gesture repetition are used for testing. k -medoids, SVM, and MDM are defined on the manifold as given in [5].

Appendix B

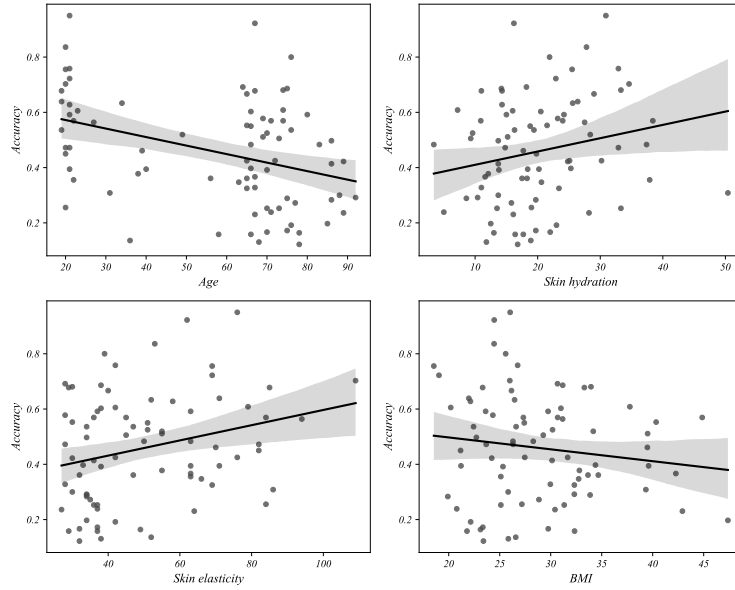


Figure 16: Regression plots of k -medoids classification accuracy with age, skin hydration, skin elasticity, and BMI for the frequency range 20 to 50 Hertz.

	Coefficient	Standard error	t	P> t
Age	-0.0571	0.031	-1.840	0.070
Skin hydration	0.0132	0.023	0.574	0.567
Skin elasticity	0.0117	0.029	0.410	0.683
BMI	-0.0125	0.022	-0.558	0.578

Table 7: Regression model values for frequency range 20 to 50 Hertz.

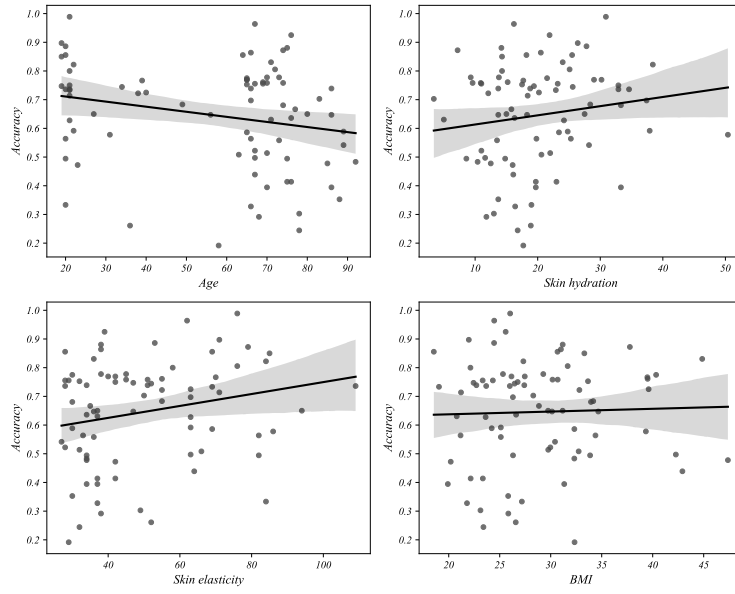


Figure 17: Regression plots of *k*-medoids classification accuracy with age, skin hydration, skin elasticity, and BMI for the frequency range 50 to 110 Hertz.

	Coefficient	Standard error	t	P> t
Age	-0.0307	0.030	-1.020	0.311
Skin hydration	0.0103	0.022	0.459	0.647
Skin elasticity	0.0161	0.028	0.582	0.562
BMI	0.0137	0.022	0.628	0.532

Table 8: Regression model values for frequency range 50 to 110 Hertz.

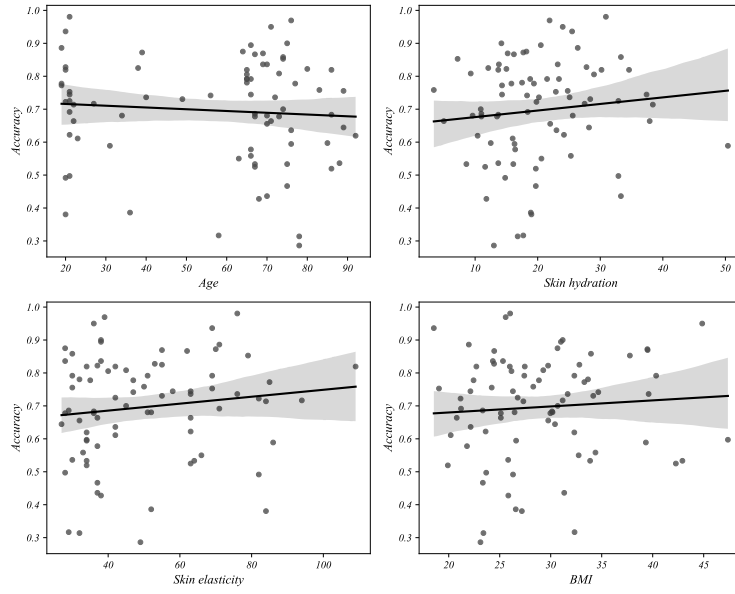


Figure 18: Regression plots of *k*-medoids classification accuracy with age, skin hydration, skin elasticity, and BMI for the frequency range 110 to 230 Hertz.

	Coefficient	Standard error	t	P> t
Age	0.0004	0.027	0.013	0.990
Skin hydration	0.0129	0.020	0.651	0.517
Skin elasticity	0.0162	0.025	0.662	0.510
BMI	0.0115	0.019	0.599	0.551

Table 9: Regression model values for frequency range 110 to 230 Hertz.

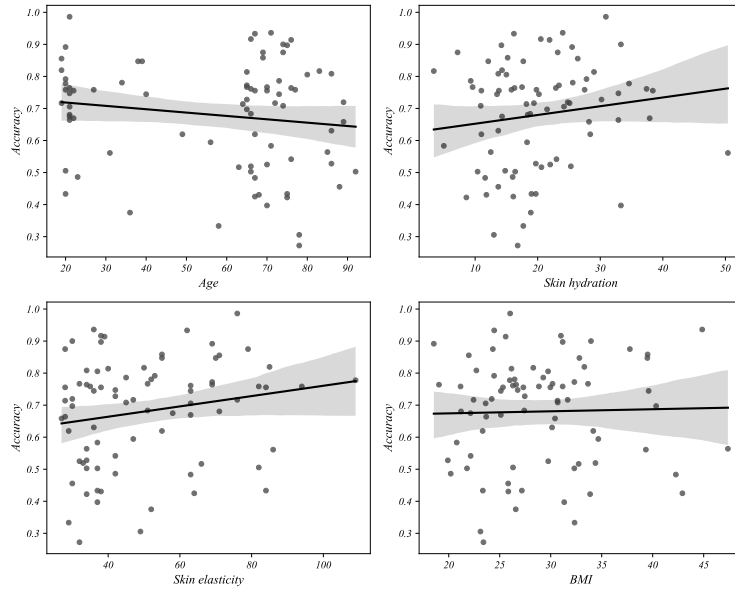


Figure 19: Regression plots of *k*-medoids classification accuracy with age, skin hydration, skin elasticity, and BMI for the frequency range 230 to 450 Hertz.

	Coefficient	Standard error	t	P> t
Age	-0.0053	0.028	-0.191	0.849
Skin hydration	0.0146	0.021	0.706	0.482
Skin elasticity	0.0228	0.026	0.888	0.377
BMI	0.0054	0.020	0.267	0.790

Table 10: Regression model values for frequency range 230 to 450 Hertz.